



Nucleation and condensational growth to CCN sizes during a sustained pristine biogenic SOA event in a forested mountain valley

J. R. Pierce¹, W. R. Leaitch², J. Liggitto², D. M. Westervelt³, C. D. Wainwright¹, J. P. D. Abbatt⁴, L. Ahlm⁵, W. Al-Basheer², D. J. Cziczo⁶, K. L. Hayden², A. K. Y. Lee⁴, S.-M. Li², L. M. Russell⁵, S. J. Sjostedt², K. B. Strawbridge², M. Travis², A. Vlasenko², J. J. B. Wentzell², H. A. Wiebe², J. P. S. Wong⁴, and A. M. Macdonald²

¹Department of Physics and Atmospheric Science, Dalhousie University, Halifax, Nova Scotia, Canada

²Environment Canada, Toronto, Ontario, Canada

³Department of Civil and Environment Engineering, Carnegie Mellon University, Pittsburgh, PA, USA

⁴Department of Chemistry, University of Toronto, Toronto, Ontario, Canada

⁵Scripps Institution of Oceanography, University of California-San Diego, La Jolla, CA, USA

⁶Department of Earth, Atmospheric and Planetary Sciences, Massachusetts Institute of Technology, Boston, MA, USA

Correspondence to: J. R. Pierce (jeffrey.pierce@dal.ca)

Received: 9 October 2011 – Published in Atmos. Chem. Phys. Discuss.: 21 October 2011

Revised: 3 March 2012 – Accepted: 26 March 2012 – Published: 2 April 2012

Abstract. The Whistler Aerosol and Cloud Study (WACS 2010), included intensive measurements of trace gases and particles at two sites on Whistler Mountain. Between 6–11 July 2010 there was a sustained high-pressure system over the region with cloud-free conditions and the highest temperatures of the study. During this period, the organic aerosol concentrations rose from $<1 \mu\text{g m}^{-3}$ to $\sim 6 \mu\text{g m}^{-3}$. Precursor gas and aerosol composition measurements show that these organics were almost entirely of secondary biogenic nature. Throughout 6–11 July, the anthropogenic influence was minimal with sulfate concentrations $<0.2 \mu\text{g m}^{-3}$ and SO_2 mixing ratios $\approx 0.05\text{--}0.1$ ppbv. Thus, this case provides excellent conditions to probe the role of biogenic secondary organic aerosol in aerosol microphysics. Although SO_2 mixing ratios were relatively low, box-model simulations show that nucleation and growth may be modeled accurately if $J_{\text{nuc}} = 3 \times 10^{-7} [\text{H}_2\text{SO}_4]$ and the organics are treated as effectively non-volatile. Due to the low condensation sink and the fast condensation rate of organics, the nucleated particles grew rapidly ($2\text{--}5 \text{ nm h}^{-1}$) with a 10–25 % probability of growing to CCN sizes (100 nm) in the first two days as opposed to being scavenged by coagulation with larger particles. The nucleated particles were observed to grow to ~ 200 nm after three days. Comparisons of size-distribution with CCN data show that particle hygroscopicity (κ) was ~ 0.1 for particles larger 150 nm, but for smaller particles near 100 nm the κ value decreased near midway through the period from 0.17 to less than 0.06. In this environment of little anthropogenic influence and low SO_2 , the

rapid growth rates of the regionally nucleated particles – due to condensation of biogenic SOA – results in an unusually high efficiency of conversion of the nucleated particles to CCN. Consequently, despite the low SO_2 , nucleation/growth appear to be the dominant source of particle number.

1 Introduction

Atmospheric aerosols affect climate directly by scattering and absorbing radiation and indirectly by influencing cloud properties (Forster et al., 2007). This indirect effect of aerosols on clouds occurs because cloud droplets form on an atmospheric particles. Increasing aerosol concentrations increases cloud droplet number concentrations and leads to clouds that are more reflective to sunlight (Twomey, 1977) and with potentially longer lifetimes (Albrecht, 1989). Both the direct and indirect effect of aerosols on climate represent the largest uncertainties in radiative forcing change that were quantified by the Intergovernmental Panel on Climate Change (IPCC) (Forster et al., 2007).

The subset of aerosols on which cloud droplets form are called cloud condensation nuclei (CCN). Whether or not a particle acts as a CCN depends on its size, composition and the maximum supersaturation of water reached within the cloud. Typically particles must have dry diameters of 50 nm or larger to nucleate cloud droplets (e.g. Seinfeld and Pandis, 2006). For moderate cloud supersaturations of 0.2 %, hygroscopic aerosols roughly 80 nm and larger will act as CCN,

whereas more hydrophobic aerosols must be larger (e.g. Petters and Kreidenweis, 2007). CCN are formed either when particles that are large and sufficiently hygroscopic are emitted directly to the atmosphere or when particles of smaller sizes grow to sufficiently sized particles through condensation of sulfuric acid and secondary organic material (e.g. Pierce and Adams, 2009a).

Aerosol nucleation (the formation of new particles from the clustering of low-volatility vapors) is the dominant source of particle number in the atmosphere (Kulmala et al., 2004; Kulmala and Kerminen, 2008) and under the right conditions can lead to the formation of many CCN (Lihavainen et al., 2003; Kerminen et al., 2005; Laaksonen et al., 2005; Merikanto et al., 2009; Makkonen et al., 2009; Pierce and Adams, 2009a; Spracklen et al., 2010; Wang and Penner, 2009; Yu and Luo, 2009). Nucleation occurs when sulfuric acid and other condensable vapors (e.g. low-volatility organics, ammonia and water) are in high-enough concentrations such that they may collide to form stable clusters before re-evaporating (Kulmala and Kerminen, 2008). These stable clusters have diameters around 1 nm, thus they must grow to CCN sizes by condensation of more vapor. However, these small, ultrafine particles are highly susceptible to coagulation scavenging by larger particles. Thus there is a competition between growth and coagulation to determine if a newly formed particle will grow to become a CCN (Pierce and Adams, 2007). Analyses by Kuang et al. (2009) and Westervelt et al. (2011) showed that generally less than 10 % of nucleated particles survive to grow to diameters of 100 nm, with some exceptional cases when more than 50 % survived to grow to 100 nm. There is, however, still substantial uncertainty in the contribution of nucleation to the global budget of CCN and the effects of aerosols on clouds and climate.

A major uncertainty in the connection between aerosols and climate is biogenic secondary organic aerosol (SOA) where volatile organic compounds (VOCs) emitted by plants are oxidized in the atmosphere to form lower volatility compounds that contribute to particle mass (e.g. Hallquist et al., 2009). The total amount of SOA formed in the atmosphere is highly uncertain and estimates published in the literature range from 12 Tg yr⁻¹ (Kanakidou et al., 2005) to 1640 Tg yr⁻¹ (Goldstein and Galbally, 2007). Further complicating the influence of SOA on climate is that the ability of condensing secondary organic matter to grow ultrafine particles to CCN sizes depends greatly on the SOA volatility. Lower-volatility SOA is able to grow freshly nucleated particles more effectively than semi-volatile SOA (Riipinen et al., 2011; Pierce et al., 2011). Additionally, the hygroscopicity of biogenic SOA is uncertain and tends to vary with the age of the aerosol (Chang et al., 2010). Therefore, atmospheric observations of SOA formation contributing to the growth of ultrafine particles to CCN sizes are necessary for understanding the effect of SOA on climate. Since SOA has been observed to be the dominant condensing species onto freshly nucleated particles in remote continental regions (Riipinen et

al., 2011), we must understand SOA condensation to understand the connection between nucleation and CCN, clouds and climate.

In this paper, we perform a detailed analysis of a 5-day event at Whistler, British Columbia, Canada where the sub-micron aerosols were dominated by biogenic SOA. This SOA was the dominant contributor to the growth of fresh ultrafine aerosols.

2 Aerosol event description

In this paper, we analyze measurements of nucleation and growth to CCN sizes during an extended period of largely natural conditions in a mountain valley in western Canada. The measurements took place during the 2010 Whistler Aerosol and Cloud Study (WACS 2010). This event occurred between 5 and 10 July 2010 when a high-pressure system moved air from the North Pacific into northern British Columbia bringing clean air to Whistler from the north that had subsided from higher altitudes. The meteorology and other general features of this event is discussed in detail in Macdonald et al. (2012). During this time period, new-particle formation events occurred and significant amounts of biogenic SOA was formed. The event was also characterized by low amounts of SO₂ and sulfate. The air mass is generally constant throughout this 5–6 day period, and aerosol mass and number concentrations evolve in a relatively smooth and continuous manner. This consistency makes this event ideal for identifying biogenic SOA properties and the role of this SOA in aerosol microphysics.

Figures 1 and 2 provide motivation for the research performed in this paper. Figure 1 shows the temperature and organics measured by an Aerosol Mass Spectrometer (AMS) for the entire WACS 2010 period at Raven's Nest, a measurement site located about half way between the valley and the peak of Whistler Mountain. Organic concentrations tend to correlate with temperatures throughout the campaign, which is evidence to the biogenic SOA being the predominant organic component at Whistler in the summertime (Macdonald et al., 2012). The effect of temperature on the SOA-precursor emissions (increasing emissions with increasing temperature) is stronger than the thermodynamic effect of temperature on SOA partitioning (decreasing SOA with increasing temperature). Thus, temperature and SOA are positively correlated, consistent with Leitch et al. (2011), which explored the temperature dependence of SOA at Whistler and Egbert (another forested Canadian location). Figure 1 shows increasing temperature and organic aerosol concentrations during the event period described above (5–10 July).

Figure 2 shows the time series of aerosol mass concentrations from Aerosol Mass Spectrometers (AMSs) and measured size distributions from Scanning Mobility Particle Sizers (SMPSs) at the peak of Whistler mountain as well as at the Raven's Nest site. Also included are the total particle

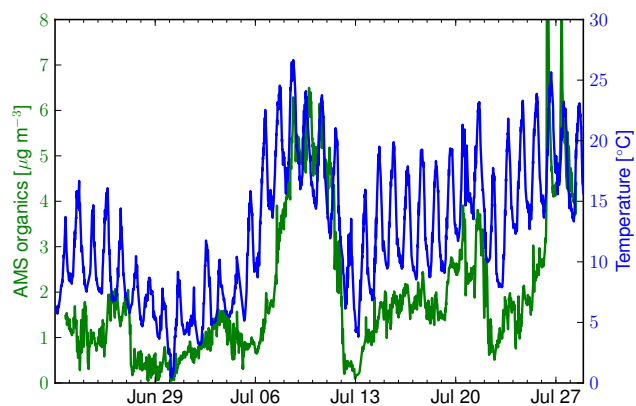


Fig. 1. Organic aerosol concentration measured by the AMS at Raven's Nest as well as the temperature measured at Raven's Nest versus time for the entire WACS 2010 campaign. The x-axis represents local Pacific daylight time.

concentrations (of particles with diameters larger than 3 nm) at the peak measured by a condensation particle counter. The plot extends from 5 July through 9 July, and in this period the air mass is generally constant. The organic aerosol concentrations steadily increase from 6 July until 9 July corresponding to the times with higher temperatures, high solar irradiance (not shown) and increasing concentrations of BVOCs in gas phase as determined by Proton Transfer Mass Spectrometry (PTR-MS) (Macdonald et al., 2012). The organic aerosols formed during the pristine event are almost entirely biogenic as determined from FTIR and mass spectroscopic analysis of the particles (Macdonald et al., 2012). Inorganic aerosol concentrations are 3–10 % of the organic concentrations from 6 July through 10 July; thus, this experiment provides a unique opportunity to determine the properties of biogenic secondary organic aerosol and their effects on ultrafine particles.

Even though sulfate concentrations appear to stay low throughout the event, new-particle events (particles show up in SMPS measurements at around 30 nm) occur strongly on 5 and 6 July. Similar but weaker events appear to exist on 7–9 July. Whatever the source of the new particles, their growth to diameters larger than 100 nm (which we will show were CCN active) is clear in Fig. 2. Thus, this case shows direct observation of growth of ultrafine particles to CCN sizes by biogenic SOA formation in a relatively unpolluted environment.

The goal of this case study is to understand the processes that shaped aerosol size and composition during this extended period of constant air mass and minimal anthropogenic influence, and to compare these results to other locations. The questions we will address are as follows:

- What processes determine the timing of the observed new-particle events? Are these events due to nucleation occurring in the boundary layer, residual layer

or free troposphere? Is the dependence of nucleation on sulfuric-acid vapor at the Whistler mountain valley consistent with observations in other remote continental sites?

- What fraction of the new particles is growing to become CCN and how does this compare to other locations?
- What is the hygroscopicity of these CCN that are comprised almost entirely from biogenic SOA? What is the volatility of the condensed SOA?

In Sect. 2, we describe the instrumentation and models used in this paper followed by the results in Sect. 3 and the conclusions in Sect. 4.

3 Methods

3.1 WACS 2010 instrumentation

The Whistler Aerosol and Cloud Study 2010 (WACS 2010) was performed between 22 June and 28 July 2010 on Whistler Mountain, Whistler, British Columbia, Canada. Instrumentation was located at three sites on or around the mountain: (1) Whistler Village at the foot of the mountain at 665 m a.s.l., (2) Raven's Nest, a mid-mountain restaurant during ski season, at 1300 m a.s.l., and (3) Whistler peak at 2182 m a.s.l. Details on the locations and instrumentation are given in (Macdonald et al., 2012), but we briefly summarize the measurements used in this paper.

A TSI Inc. Scanning Mobility Particle Sizer (SMPS), comprised of a 3081L electrostatic classifier and a 3775 Condensation Particle Counter, was used to measure particle size distributions between diameters of 16 nm and 685 nm at Raven's Nest. The distributions were analyzed with TSI software based on Wang and Flagan (1990). At the Peak, there were instruments in two locations: the on-going measurement facility (e.g. Macdonald et al., 2011) is in the basement of the lift operator building, and in a shipping container positioned adjacent to the lift operator's building for the 2010 study in order to house additional instruments. In the basement location, there was a SMPS (same model components as at Raven's Nest) that measured particle size distributions from 14 nm to 573 nm and a TSI Ultrafine Condensation Particle Counter (3025 UCPC) for total particle number concentrations >3 nm. Particles concentrations from 350 nm to 10 μm were measured using a Grimm 1.109 optical particle counter. In the container, total particle number concentrations were measured with a TSI 3775 CPC and particle size distributions from 15 nm to 10 μm diameter were measured with a MSP Inc. Wide-range Particle Spectrometer (WPS; Liu et al., 2010). The WSP combines a Scanning Mobility Spectrometer for particle measurement from 15–500 nm and a Laser Particle Spectrometer for measurement in the 0.5 to 10 μm range. The LPS data are based on the manufacturer's calibration using polystyrene latex particles (PSLs; real refractive

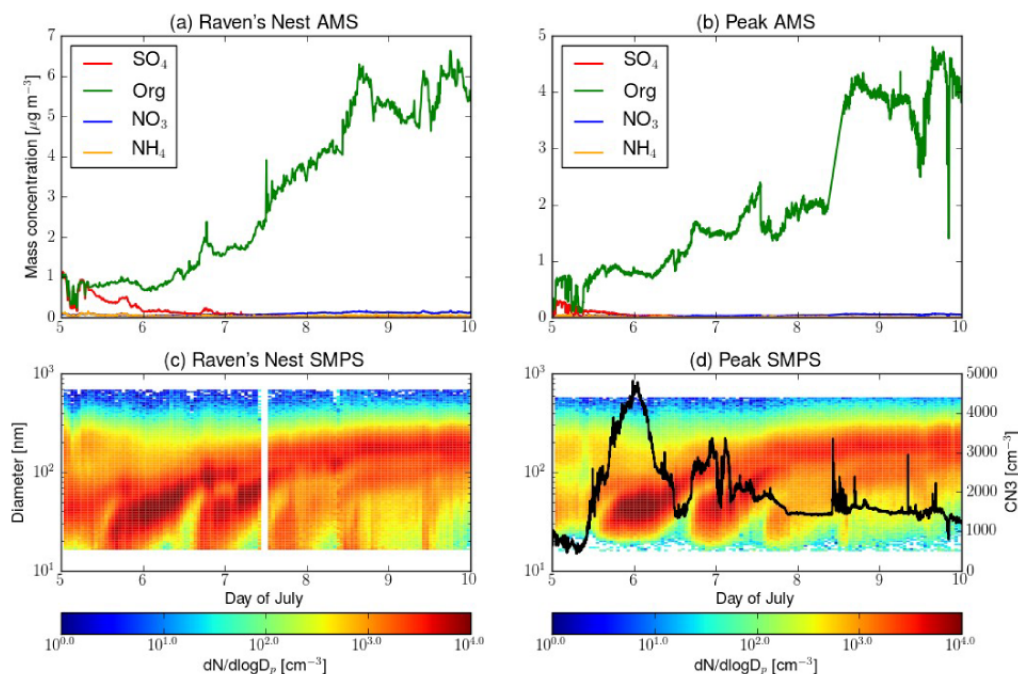


Fig. 2. (a) AMS mass timeseries at Raven's Nest. (b) AMS mass timeseries at Peak. (c) SMPS size distribution timeseries at Raven's Nest. (d) SMPS size distribution timeseries at Peak with the total number of particles with diameters larger than 3 nm (CN3) measured by a CPC (black line) during the same period. The x-axes represent local Pacific daylight time.

index of 1.585). A DMT UHSAS, which measures the particle number distribution from 60 nm to 1 μm , was also part of the container instrumentation. The SMPS distributions at both the Nest and Peak sites were adjusted for the appropriate mean free paths and corrected for diffusion losses and multiple charging.

The particles concentrations measured with the WSP, the SMPS and UHSAS at the Peak agreed to within 10 % across the study. Also at the Peak, a separate SMPS system was used as a classifier for generating monodisperse particles for calibration of other systems three times during the study. The sizing of the SMPS was checked with PSLs of 100 nm and 350 nm diameter, and found to be within 10 % of the nominal value of the PSL. At Raven's Nest, calibrations of the AMS and SMPS were done with nearly monodisperse particles selected using a BMI Inc. Scanning Electrical Mobility Spectrometer.

Size resolved aerosol mass concentrations of non-refractory components of particles in the size range of 100–700 nm vacuum aerodynamic diameter (these values correspond to ~ 50 % cut points based on Liu et al. (2010), but qualitative measurements are made outside of this range) were measured at Raven's Nest using an Aerodyne Research Inc. High Resolution time-of-flight Aerosol Mass Spectrometer (HR-tof-AMS; Drewnick et al., 2005; DeCarlo et al., 2008, 2006) and at the Peak using a C-ToF AMS (Jayne et al., 2000; Jimenez et al., 2003; Drewnick et al., 2005;

Canagaratna et al., 2007). Based on comparison with the SMPS volume distributions and the FTIR filter OM (Macdonald et al., 2012), the collection efficiency of the AMS was found to be close to unity at Raven's Nest and approximately 0.5 at Whistler Peak. The collection efficiencies were found to be nearly constant in time at each location. These corrections are applied to the AMS data shown here.

At Raven's Nest only, cloud condensation nucleus (CCN) concentrations were measured using a Droplet Measurement Technologies (DMT) Cloud Condensation Nucleus Counter model 200 (dual channel) developed by Roberts and Nenes (2005). One column was used to step between 5 supersaturations (0.07 %, 0.1 %, 0.2 %, 0.3 % and 0.5 %) with 6-min intervals while another column was held fixed at 0.2 % supersaturation and used for aerosol oxidation experiments. The results of the oxidation experiments are given in Wong et al. (2011).

SO_2 mixing ratios were measured at Raven's Nest and the Peak using TECO 43i and TECO 43c trace level analyzers, respectively. Ozone concentrations were monitored at Raven's Nest and the Peak using TECO 49c and TECO 49i, respectively. The instruments for SO_2 and ozone were calibrated at both sites using the same NIST traceable standards. Wind direction and speed at Raven's Nest were provided through an automated weather station through the Olympic Automated Network. We use results from a Lidar located at the Whistler Weather Station at Whistler Village. At the

time, the Lidar was part of the Canadian Operational Research Aerosol Lidar Network, and it is a dual-wavelength upward-pointing aerosol Lidar using an Nd:YAG pulsed 10-Hz Laser that is emitted at both the 1064 nm (fundamental) and 532 nm (frequency doubled) wavelengths. Data was collected in three channels, 1064, 532 polarized, and 532 depolarized.

In the basement at the Peak, the ambient particles are delivered into the instrument room through a vertical stainless steel manifold with an open intake covered above by a slightly conical hat. The flow through the 7.3 cm ID manifold is approximately 1201 min^{-1} along the 6 m length for an average residence time of about 12 s; transfer time from the manifold to each instrument is <1 s. At the end of the manifold, particles are sampled from near the centre of the flow to minimize wall losses of primarily ultrafine particles. Losses of coarse particles are primarily defined by the horizontal wind speeds at the intake point, and previous comparisons with other measurements suggest that particles of at least $6 \mu\text{m}$ diameter are sampled with efficiency equivalent to the measurement uncertainty. Ambient aerosol particles were drawn into the container at the Peak using a 0.8 cm ID stainless tube approximately 6 m in length at a flow rate of 101 min^{-1} , equivalent to a residence time of about 0.2 s. None of the particle measurements in the container included sizes $>1 \mu\text{m}$ diameter. At Raven's Nest, the tube feeding the particle measurements had an inner diameter of 0.8 cm, a length of about 10 m and a total flow rate of about 251 min^{-1} . To test for the influence of particle line losses between the sampling inlet and the size distribution measurements from the SMPS, we calculate the theoretical size-dependent losses at Raven's Nest (where the maximum losses may have occurred) using the technique of (Kumar et al., 2008). For the Raven's Nest inlet, we treated the flow as turbulent since the Reynolds number was >4000 . Accordingly, we calculate that about 95 % of 3 nm particles, 55 % of 10 nm particles, 20 % of 20 nm particles, 10 % of 40 nm particles and 3 % of 100 nm particles were removed. The implications of this are discussed later.

3.2 TOMAS box model

To investigate various nucleation and growth processes, we complement the measurements with a box model version of the Two Moment Aerosol Sectional (TOMAS) microphysics model (Adams and Seinfeld, 2002; Pierce and Adams, 2009b; Pierce et al., 2011). This model will allow us to compare nucleation and growth at Whistler to that observed in other locations, and it allows us to determine information about the volatility of the condensing SOA (Pierce et al., 2011). The most up-to-date description of the model is given in Pierce et al. (2011). Simulations were run from the start of 5 July until the end of 10 July.

This version of the TOMAS box model uses 40 logarithmically spaced size sections to represent dry diameters of 1 nm to $10 \mu\text{m}$. The modeled aerosol species (within each size section) are sulfate, water and 8 organic aerosol species representing lumped species with logarithmically spaced equilibrium vapor concentrations between 10^{-5} and $10^2 \mu\text{g m}^{-3}$ (Donahue et al., 2006). The modeled gas-phase species are sulfuric acid and the 8 gas-phase organic species with volatilities corresponding to the 8 aerosol-phase organic species. The numerics of condensation/evaporation and coagulation are discussed in Adams and Seinfeld (2002). The equilibrium vapor concentration of sulfuric acid is assumed to be negligible due to the presence of aerosol water (Seinfeld and Pandis, 2006). The organic species are assumed to create a pseudo-ideal mixture in the condensed phase (activity coefficients are constant and incorporated into the equilibrium vapor concentrations; Donahue et al., 2006). Sulfuric acid and organics undergo condensation (and evaporation in the case of organics) via kinetic mass transfer.

Organic aerosol is assumed to have ΔH_{vap} values based on Epstein et al. (2010). The molecular weight of organics is assumed to be 200 g mol^{-1} for all bins. The density of organics is assumed to be 1400 kg m^{-3} . The initial dry particle composition is assumed to be half sulfate and half organics (and water in equilibrium with this mixture). Freshly nucleated particles at 1 nm are also assumed to be half sulfate and half organics. The results and the conclusions in this paper are not strongly sensitive to the four assumptions above. Pre-existing organic aerosol is assumed to have an equilibrium vapor concentration of $10^{-5} \mu\text{g m}^{-3}$. The accommodation coefficient is assumed to be 1, and the surface tension of the aerosols is assumed to be 0.025 N m^{-1} . The model is somewhat sensitive to the assumed values of pre-existing organic volatility, accommodation coefficient and surface tension, and a detailed analysis of these three parameters is shown in Pierce et al. (2011). SOA formed during the event is assumed to have an equilibrium vapor concentration of $10^{-3} \mu\text{g m}^{-3}$ consistent with the best-fit results of Pierce et al. (2011).

H_2SO_4 vapor concentrations in the box model are inferred from in-situ SO_2 and condensation sink measurements using the method described by (Petäjä et al., 2009). In this technique, H_2SO_4 vapor is assumed to be in pseudo-steady state between gas-phase production (through oxidation of SO_2) and condensational losses:

$$[\text{H}_2\text{SO}_4] = \frac{k[\text{SO}_2]R}{\text{CS}} \quad (1)$$

In this equation, the formation of H_2SO_4 is approximated by $k[\text{SO}_2]R$, where k is an empirical constant ($2.3 \times 10^{-9} [\text{m}^2 \text{W}^{-1} \text{s}^{-1}]$) derived from data in Hyytiälä, Finland, and R is the total downwelling shortwave radiation. CS is the condensation sink [s^{-1}] (i.e. first-order condensational loss rate) that is proportional to the Fuchs corrected aerosol surface area (Kulmala et al., 2001). When calculating H_2SO_4

concentrations, we use the measured SO_2 concentrations, CS calculated from the SMPS measurements assuming an accommodation coefficient of 1, and a value of R that is approximated from solar zenith angle and assuming an atmospheric transmission of 0.76 and assuming a cloud-free atmosphere (the atmosphere was cloud-free for most of the event and uncertainties by assuming no clouds will be discussed later).

Also for the box model, we infer nucleation rates using the inferred H_2SO_4 concentrations above and the activation nucleation formulation (Sihto et al., 2006):

$$J = A[\text{H}_2\text{SO}_4] \quad (2)$$

Where J is the nucleation rate of 1 nm particles and A [s^{-1}] is an empirical constant. Literature has shown this constant to vary from 3.3×10^{-8} – $3.4 \times 10^{-4} \text{ s}^{-1}$ in regions of Europe (Sihto et al., 2006; Riipinen et al., 2007; Spracklen et al., 2008). We will use a moderate value of $3 \times 10^{-7} \text{ s}^{-1}$ and will describe the consequences of this assumption. We also tested the nucleation scheme of Metzger et al. (2010), which assumes that nucleation is dependent on the product of sulfuric acid and low-volatility organic vapor concentrations. Because both sulfuric acid and low-volatility organic formation were both correlated with sunlight during this period, there was little difference between the Metzger et al. (2010) scheme and the activation scheme. Thus, we only include the results of the activation scheme here.

We constrain the box model inputs with measurements from Raven's Nest. The initial size distribution is taken from the SMPS measurements at the start of 5 July. Figure 3 shows the measurement-derived nucleation rate, sulfuric acid and SOA formation rates (corrected for dilution) and the first-order dilution constant (by entrainment of cleaner free-tropospheric air) used for inputs to the TOMAS box model. The model-input nucleation rates were derived following the technique described in the above paragraph. The nucleated particles are added to the model at 1 nm. Sulfuric acid and organic material are added to the gas phase based on the mass change in sulfate and organic concentrations measured by the AMS (these species then condense onto the particles in TOMAS such that the aerosol masses in the model will match AMS observations). Since all SOA formed in the model has a volatility of $10^{-3} \mu\text{g m}^{-3}$ and total organic concentrations in the model are always much larger than $10^{-3} \mu\text{g m}^{-3}$, nearly all of the freshly formed organic vapors will condense to the aerosol phase to form SOA mass in the model (Donahue et al., 2006). This organic aerosol constraint ensures that the total organic aerosol mass in the model matches the concentrations measured by the AMS. Finally, particle concentrations were observed to decrease by $\sim 25\%$ during late-morning boundary-layer growth due to entrainment of free-tropospheric air (to be discussed later). To account for this, we include steady 1st-order dilution of gas and particle concentrations in the box between 09:00 and 11:00 PDT each day to reproduce this measured dilution.

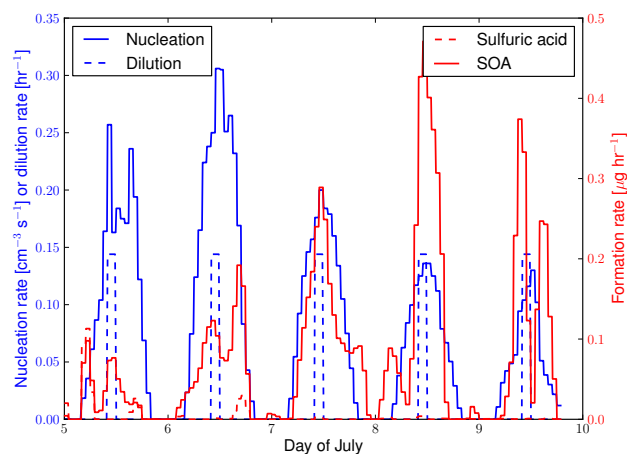


Fig. 3. Time-dependent inputs to TOMAS box model of Raven's Nest. Nucleation is estimated from SO_2 measurements, H_2SO_4 condensation sink measurements from the SMPS, and estimated total downwelling solar radiation using the method of Petäjä et al. (2009). Dilution with clean FT air is estimated from the average drop in aerosol concentrations between 09:00 and 11:00 a.m. during these 5 days measured by the SMPS. Sulfuric acid and SOA formation rates are estimated from AMS measurements and have been corrected for dilution.

4 Results

4.1 Processes controlling new-particle events

In this section, we explore the nature of the observed new-particle formation events and use clues from measured meteorology and chemistry at Whistler as well as information regarding new-particle formation at other locations to better understand the cause of these events.

4.1.1 Timing of observed new-particle formation events

In Fig. 2c and d show the aerosol size distribution time series at Raven's Nest and the Peak. On 5, 6 and 7 July, new particles clearly appear around 30 nm shortly after noon at both locations. Weaker events may be occurring on the 8 and 9 July; however, because these events appear to contribute significantly fewer particles, we will only focus on the timing of nucleation during the first three days. In this subsection, we compare the timing of these new-particle formation events relative to Lidar backscatter profiles, ozone concentrations and wind speeds to gain insight into the nature of the daily formation events.

Figure 4 shows the backscatter ratio profile from the Lidar, the ozone concentrations at Raven's Nest and the Peak as well as the wind directions at Raven's Nest over the event. Also plotted over the Lidar backscatter figure is the estimated clear-sky downwelling solar radiation as a function of time to help visualize diurnal cycles. Radiation was not measured, and these clear-sky estimates represent an upper bound for

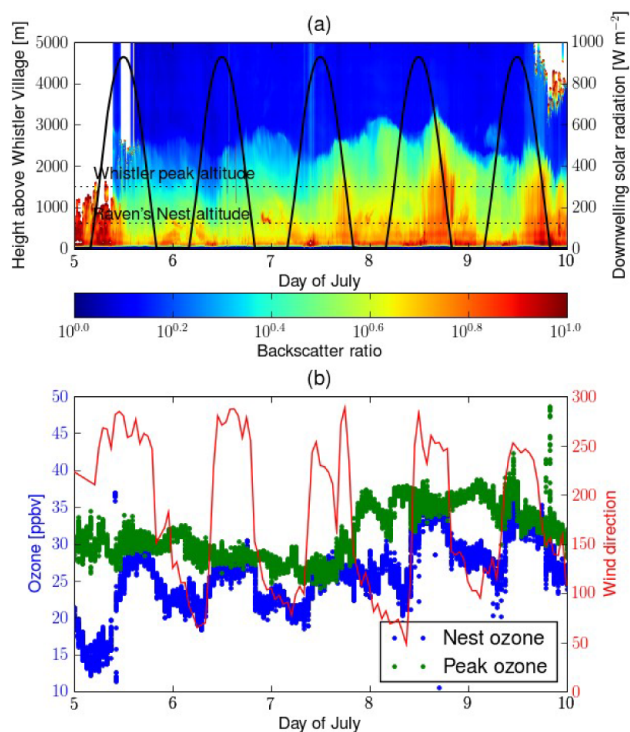


Fig. 4. (a) Lidar backscatterer ratio profile vs. height and time. Dashed black lines show the altitudes of Raven's Nest and Whistler Peak (however, mixing along the side of the mountain may be different than in the clear air above the Lidar, so these heights might not actually represent the backscatterer ratio at the two measurement sites). Solid black line and right axes shows estimated downwelling shortwave radiation at the surface. (b) Ozone timeseries at Raven's Nest and peak and wind direction at Raven's Nest.

shortwave radiation. The Lidar indicated cloud during the first half of 5 July, but no cloud again until late on 9 July. After the clouds cleared, the boundary layer in the Lidar profile (as defined by the height of elevated aerosol concentrations, the daytime mixed layer plus nighttime residual layer) varies from just under 2 km to just over 3 km above the Lidar at Whistler Village throughout the event. The mean backscatterer ratio during this time period in the boundary layer grows with time due to (1) the increasing number of particles due to the new particle events and (2) the growth of particles to sizes more effective for backscatter. Buoyancy-driven upward mixing of surface aerosols and particle growth processes enhanced by photochemistry lead to an increase in the backscatter beginning in the late morning and maximizing during the late afternoon. The late-day decrease is caused by downslope flow bringing air with lower particle concentrations into the nocturnal residual layer, as previously shown for Whistler (Gallagher et al., 2011). Figure 5a shows the diurnal cycle of the mean backscatterer ratio between 1 and 2 km above Whistler Village averaged over noon 5 July through noon 8 July. Whistler peak is roughly 1.5 km above Whistler

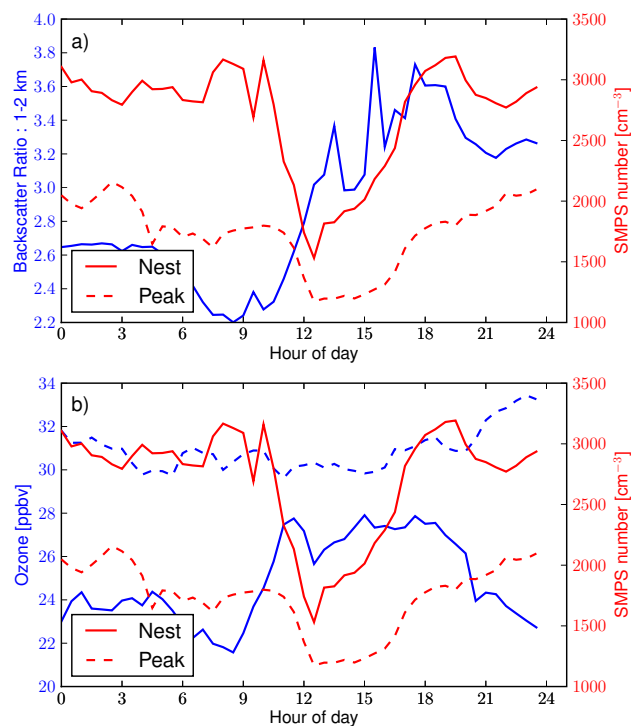


Fig. 5. Diurnal cycle averaged over 12:00 PDT 6 July through 12:00 PDT 7 July for (a) peak aerosol number from the SMPS, Raven's Nest aerosol number from the SMPS and 1–2 km Lidar backscatterer ratio. (b) The same as (a) except with ozone mixing ratios rather than Lidar backscatterer ratio.

Village; however, because atmospheric mixing close to the mountain may be different from the clear air above the Lidar, these values may not represent the actual backscatterer ratio values by the measurement station at the peak.

The wind directions at Raven's Nest in Fig. 4b show a clear diurnal cycle with a near- 180° shift between directions. This shift in wind direction is due to upslope winds during the day and downslope winds at night (Gallagher et al., 2011). During the daytime upslope winds, the ozone mixing ratios at Raven's Nest are similar to the mixing ratios measured at the peak, while at night Raven's Nest is significantly lower. The daytime increase in ozone at Raven's Nest is a combination of mixing down from the peak and photochemistry in the afternoon (Macdonald et al., 2011). This was determined from comparisons of ozone at the Nest and peak as well as OH concentrations at Raven's Nest. The reason for the overnight decrease in ozone at Raven's Nest is unclear; however, particle number concentrations do not show a decrease at night (beyond what is explained by coagulation), so this points to a chemical or depositional loss of ozone rather than a change in air mass. Figure 5b shows the diurnal cycle of ozone at Raven's Nest and Whistler peak averaged over 5 July through 7 July.

Figure 5 shows the mean diurnal cycles of the integrated particle number concentrations measured by the SMPSs (summed over all SMPS sizes) at Raven's Nest and the Peak as well as the Lidar backscatter ratio between 1–2 km and the ozone mixing ratios at Raven's Nest and the Peak. Because the SMPS only counts particles between 17–685 nm, this is a lower-bound value for total number. Diurnal cycles are averaged from 12:00 Pacific Daylight Time (PDT) 5 July through 12:00 8 July (the morning of 5 July is not used to avoid the influence of the low clouds). Particle number concentrations at Raven's Nest decrease by about 25 % between 10:00–12:00 PDT. Particle number concentrations at the Peak also drop by a smaller amount around the same time. This corresponds to the same time that the surface aerosols begin to mix into the 1–2 km range of the Lidar. This is evidence that strong buoyancy-driven turbulent mixing is beginning around this time diluting the concentrations of aerosol at the surface. The Raven's Nest ozone concentrations begin to increase about 1 h earlier than the mixing shown by the Lidar. However, turbulent mixing of the air on the side of the mountain may be earlier than in the air above the Lidar. Therefore, it is unclear if the early increase in ozone at Raven's Nest was caused by mixing down of air at the elevation of the peak or was photochemically driven.

New particles show up at both locations around 15:00 PDT, which is about 5–6 h after the apparent start of turbulent mixing. This time does not correspond with any significant change in the ozone measurements. However, the Lidar backscatter is still increasing at this time and the mixed-layer height is generally increasing during the late afternoon (Fig. 4a). Thus, there is some evidence from these data that the 30 nm particles may be directly being entrained from the free troposphere or from the nighttime residual layer during the afternoon. It is also possible that particles are formed in the residual layer or free troposphere, mixed into the boundary layer earlier in the day (10:00–12:00 PDT) when they are still small (e.g. smaller than 10 nm), and then grown in the boundary layer. However, we do not have conclusive evidence for either of these scenarios. In the next section we explore the growth of the particles in the boundary layer and the possibility that nucleation was occurring directly in the boundary layer.

4.1.2 Is nucleation occurring in the boundary layer?

In this section, we use the TOMAS box model – constrained by observations at Raven's Nest – to explore nucleation and growth in the boundary layer. Figure 6 shows SO_2 concentrations at Raven's Nest. SO_2 concentrations at Raven's Nest are generally close to the measurement detection limit (0.05 ppbv) between 5 July and 8 July with occasional spikes to higher values. The two main spikes in SO_2 concentration occur in the late afternoon on 5 and 6 July roughly corresponding to the times where the new particles arrive on these two days (note that there are not increases in SO_2 during the

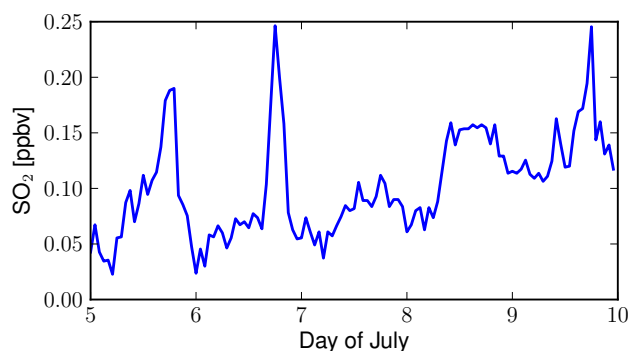


Fig. 6. Measured SO_2 mixing ratios at Raven's Nest.

times when new particles arrive on the later days). There are at least two potential sources for the small increases in SO_2 :

1. The main regional source is most likely a pulp mill 75 km west-southwest of Whistler (<http://www.ec.gc.ca/inrp-npri/default.asp?lang=en&n=1D892B9F-1#npri>). When valley winds are westerly to southerly, the air from the pulp mill can be channeled to Whistler via the mountain valley. Later in the study, larger increases in SO_2 were associated with winds from the direction of the pulp mill (Macdonald et al., 2011, 2012). At the beginning of this main biogenic period the synoptic winds were north-westerly to north-easterly, which suggests that the influence of this source was likely to have been minimal.
2. The Karymski volcano in Kamchatka was active during this period with eruptions that produced ash plumes to 7 km elevation on 11 June 2010 and 1 July 2010. Back trajectories arriving at Whistler Peak on 00:00 6 July 2010 extend back to the Kamchatka Peninsula on 29 June 2010 (not shown), leaving the possibility that out gassing of the volcano was responsible for the increased (though still low) SO_2 at Whistler during 5–7 July.

However, throughout most of the period of interest, the SO_2 mixing ratios are generally around 0.05 ppbv, so we will use this as our assumed boundary layer mixing ratio in the model.

Figure 7 illustrates the process of calculating the H_2SO_4 concentrations and associated activation nucleation rates from the measured SO_2 and condensation sink and the estimated solar flux using the method of Petäjä et al. (2009). Panel (a) shows the estimated clear-sky solar flux described in the measurements section. Since we have no direct measurements, the values are identical for each day regardless of cloud cover. The Lidar measurements showed that clouds were present before 09:00 a.m. and between 11:00 a.m. and 03:00 p.m. (broken clouds) on 5 July, and after 03:00 p.m. on 9 July. However, since we do not have direct radiation measurements, we ignore the influence of clouds on the radiation, and this will add uncertainty to the nucleation predicted

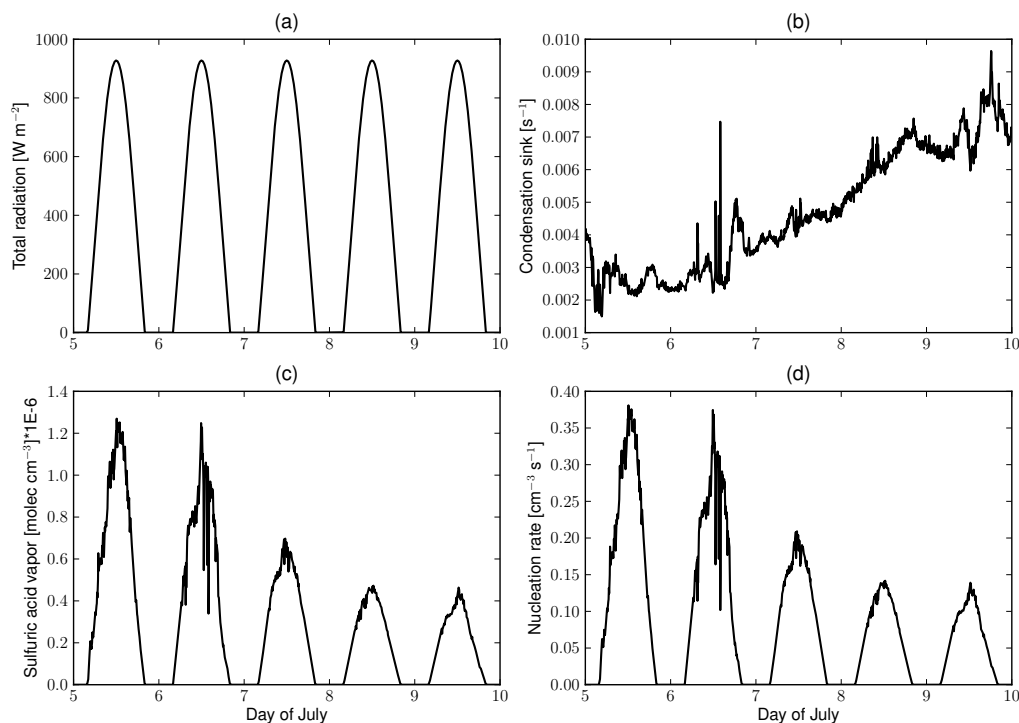


Fig. 7. (a) Estimated global radiation vs. time. (b) Condensation sink (measured) vs. time. (c) Estimated H_2SO_4 concentration (using the method of Petäjä et al., 2009) vs. time. SO_2 concentration was assumed to be 0.05 ppbv. (d) Estimated nucleation rate ($J = 3 \times 10^{-7}$ [H_2SO_4]) vs. time.

during these time periods. Panel (b) shows the condensation sink calculated from the Raven's Nest SMPS. The condensation sink steadily increases from 6 July until 9 July as the new particles grow to accumulation-mode sizes. The condensation sink on 9 July is about three times larger than the condensation sink on 5 July. Panel (c) shows the estimated H_2SO_4 concentrations from the Petäjä method. The maximum daily H_2SO_4 concentration drops by a factor of three between 5 July and 8 July. This is because although SO_2 concentrations (Fig. 6) and the diurnal cycle of solar radiation are assumed to be exactly constant, the condensation sink of H_2SO_4 triples during this time. Estimated nucleation rates (panel d) are a linear function of H_2SO_4 concentrations and thus show the same behavior. The maximum nucleation rate is $0.38 \text{ cm}^{-3} \text{ s}^{-1}$ on 5 July. These nucleation rates are similar to the median J_3 values (particle formation rate at 3 nm) measured on nucleation-event days at Hyytiälä, Finland (Westervelt et al., 2011; Dal Maso et al., 2005). Thus, since the nucleation rates used here are the particle formation rates at 1 nm, our J_3 values would be somewhat lower. We test these estimated nucleation rates in the TOMAS box model to determine if the observed new-particle formation and growth are recreated. This test will show if similar physics governing nucleation in the boundary layer in Hyytiälä, Finland may be responsible for the observed new particles at 30 nm (since we assume the H_2SO_4 and nucleation dependencies based on parameterizations from Hyytiälä, Finland).

Figure 8 shows the measured (panel a) and modeled (panel b) size distributions at Raven's Nest from 5 July through 10 July. Also included are the modeled size distributions with modeled particle losses in the sampling lines at Raven's Nest (panel c). Comparing panels (a) and (b) shows that the estimated nucleation rates could largely account for the new particles in the model. Figure 9 shows the measured (summed over SMPS sizes) and modeled number of particles with diameters less than and greater than 100 nm. To allow for comparison with the measurements, 17 nm is used for the lower cutoff for the model when calculating the number of ultrafine particles. The model captures the general behavior of the ultrafine particles, although it underpredicts ultrafine particle concentrations by about 30% on average during the evening of 5 July and the morning of 7 July. The evolution of accumulation-mode number ($D_p > 100 \text{ nm}$) is captured well by the model. In both the measurements and model, any decrease in concentration of these particles due to dilution in the late morning is compensated by growth of smaller particles into the size range. In Fig. 9, the modeled new particles show up 1–2 h earlier than the measurements on 5 July and, to a lesser degree, on 6 July. This may be due to the simple radiation scheme used in determining the H_2SO_4 concentrations that does not account for the morning clouds on 5 July and the nearby mountains blocking morning sunlight.

In our analysis, we assumed that the A-factor for activation nucleation (Sihto et al., 2006) was $3 \times 10^{-7} \text{ s}^{-1}$. This value

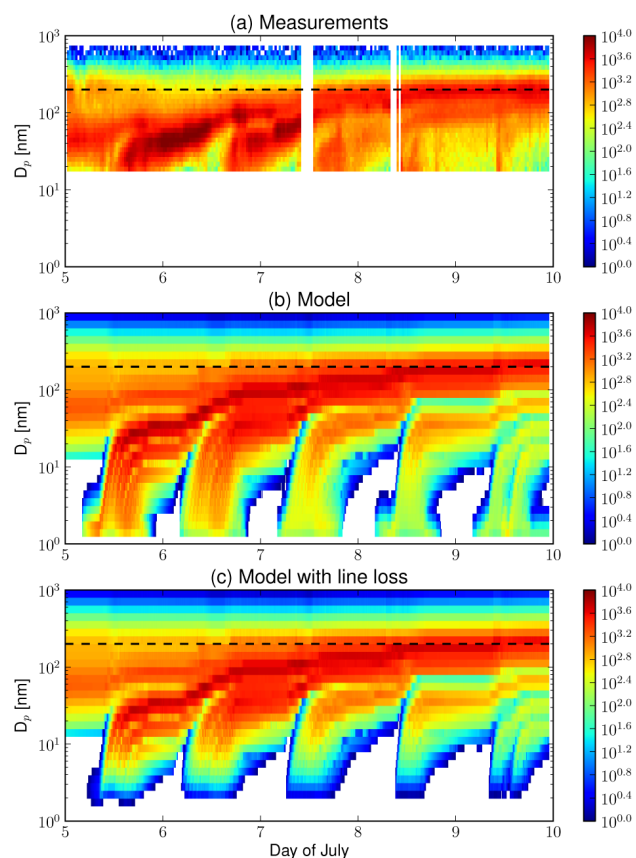


Fig. 8. (a) Measured SMPS size distribution ($\text{dN}/\text{dlog}D_p [\text{cm}^{-3}]$) at Raven's Nest vs. time. (b) Simulated size distributions vs. time. (c) Simulated size distributions with simulated sampling-line losses vs. time.

is within the range of observed values in continental Europe, 3.3×10^{-8} – $3.4 \times 10^{-4} \text{ s}^{-1}$ (Sihto et al., 2006; Riipinen et al., 2007), and within the smaller range more typically used in modeling studies, 1×10^{-7} – $2 \times 10^{-6} \text{ s}^{-1}$ (Merikanto et al., 2009; Wang and Penner, 2009; Stevens et al., 2012). Sensitivity studies (not shown) were done where the A-factor was varied from 1×10^{-7} – $1 \times 10^{-6} \text{ s}^{-1}$. These values led to a general underprediction and overprediction of the concentration of particles smaller than 100 nm, respectively. However, the concentration of particles larger than 100 nm did not change greatly due to microphysical feedbacks (slower nucleation leads to a higher probability of growth to larger sizes, Pierce and Adams, 2009a). Regardless, if nucleation was the source of the observed new particles, the nucleation rates are similar to other continental observations under similar conditions.

The model indicates that nucleation in the mixed layer can account for the observed new particles, but the question that remains is why the particles were first observed around 30 nm rather than 17 nm, the lowest detected size by the SMPS. This might be explained by nucleation having taken place in a different location than where the measurements

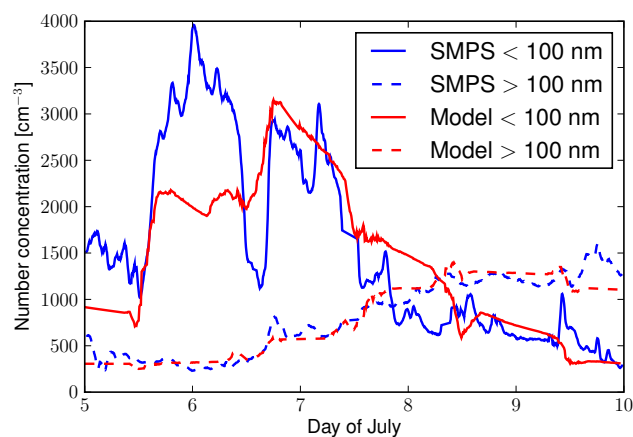


Fig. 9. Modeled and measured (Raven's Nest) total particles with $16 \text{ nm} < D_p < 100 \text{ nm}$ and total particles with $D_p > 100 \text{ nm}$ vs. time. 16 nm is the lower size cutoff of the SMPS at Raven's Nest.

were made. An obvious possibility is the entrainment of 30 nm particles from the residual layer or free troposphere as was discussed in the last section. Another possibility is that nucleation and growth may have occurred in the valley below Whistler, but these particles did not mix up to the higher-altitude measurement sites until upslope mixing was strong in the afternoon. However, the increase in CN3 at the peak (Fig. 2d) precedes the increase in the 30 nm particles at the Peak by about 3 h on 5 July and 1 h on 6 July, and the CN3 concentrations are about 10–20 % higher than the total number concentrations measured with the SMPS during the nucleation event on 5 July and 30 % larger during the events; unfortunately, there was no stand-alone CPC at Raven's Nest. The comparison of the CN3 and SMPS at the Peak indicates that the reduction of particles smaller than 30 nm in the SMPS may be instrument or sampling related and that particles smaller than 30 nm were actually in the boundary layer. Figure 8c shows the modeled size distributions as a function of time when the estimated size-dependent line losses at Raven's Nest are included. This correction visibly lowers the number of particles smaller than 20 nm, but the calculated line losses above $\sim 20 \text{ nm}$ are not large enough to account for the observed decrease in particle concentrations between 20–30 nm. Also, the CN3 were sampled off the same line as the SMPS, which suggests that the sampling lines were not the primary cause. Also, comparisons of the particle measurements between the container and the basement at the Peak do not indicate differences despite significant differences in the sampling configurations.

Thus, we cannot conclude if the source of the 30 nm particles were due to (1) nucleation throughout the day in the mixed layer (including the regions around Raven's Nest and the peak), (2) in the mixed layer in the morning with subsequent mixing up to Raven's Nest and the peak in the afternoon or (3) entrainment from the residual layer or free troposphere.

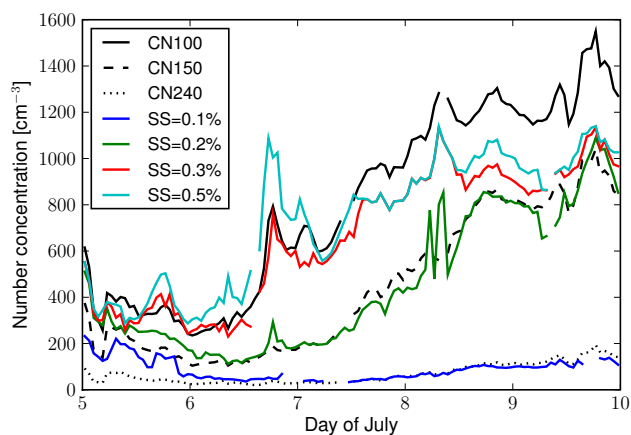


Fig. 10. Measured CCN concentrations at 4 supersaturations (colored lines) and CN100, CN150 and CN240 (number concentrations of particles larger than 100, 150 and 240 nm, respectively; black lines) at Raven's Nest versus time.

4.2 SOA volatility

The measurement-constrained TOMAS box model also allows us to gain some insight about the mean volatility of the organic aerosol condensing onto the ultrafine particles. Riipinen et al. (2011) and Pierce et al. (2011) showed that new-particle growth occurs much more rapidly when the saturation vapor concentration of condensing organics is effectively non-volatile (saturation vapor concentration around 10^{-3} to 10^{-2} $\mu\text{g m}^{-3}$ or less) because they tend to net-condense to aerosol surface area without re-evaporating. Semi-volatile organics (saturation vapor concentrations around 10^{-1} to 10^1 $\mu\text{g m}^{-3}$) cycle between the aerosol and gas phases on timescales generally shorter than aerosol growth, which allows equilibrium partitioning of SOA mass to the pre-existing aerosol mass. Thus, since freshly nucleated aerosols contain negligible mass relative to larger particles, there is very little net condensation of semi-volatile SOA mass into these freshly formed particles. Freshly nucleated particles will generally not grow if semi-volatile SOA is the only condensable material (Pierce et al., 2011).

In the TOMAS box model, we assumed that the saturation vapor concentration of SOA was 10^{-3} $\mu\text{g m}^{-3}$ (effectively non-volatile), and the growth of the particles was predicted well. We also ran simulations where the saturation vapor concentration was 10^{-2} and 10^{-1} $\mu\text{g m}^{-3}$ (not shown). These simulations corresponded to less growth than the observed nucleation modes and no growth of the nucleation modes, respectively. These results show that the organics in growing ultrafine particles in Whistler must have average saturation vapor concentrations less than 10^{-2} $\mu\text{g m}^{-3}$. These results are similar to analysis of nucleation/growth events at Hyytiälä, Finland and Egbert, Ontario, Canada in Pierce et al. (2011). For a more detailed analysis of

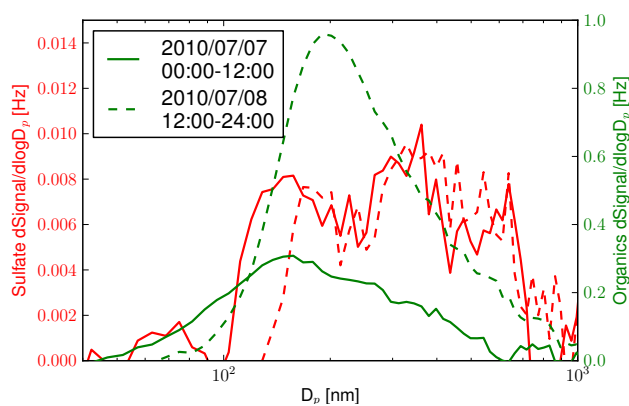


Fig. 11. Size-resolved sulfate and organic signal from the AMS at Raven's Nest for the morning of 7 July and the evening of 8 July. The x-axis represents geometric diameter (converted from vacuum aerodynamic diameter assuming a density of 1300 kg m^{-3}). The average deviation in the PToF signal across the size distribution is approximately 0.0019 Hz, which implies that changes in organics throughout the entire size range and sulfate from 100–600 nm may be reliably detected (at least qualitatively). Organics have increased in size and in total mass. The total mass of sulfate has remained essentially constant, but it has grown to larger sizes due to condensation of organics. While there was sulfate signal for 100–150 nm particles above the detection limit during the early time, there was no significant sulfate signal in this size range during the later time. The timing of this shift in sulfate sizes corresponds to the lowering of κ in the 100-nm particles.

uncertainties and discussion of implications, please refer to Pierce et al. (2011). These results also agree with the results of Westervelt et al. (2011), which assumed non-volatile SOA condensation and reproduced nucleation-mode growth rates at 6 locations in a 3-D chemical transport model. These volatilities are quite low (saturation vapor concentrations less than 10^{-2} $\mu\text{g m}^{-3}$), and it is not clear from this analysis (1) whether the volatilities became this low from gas-phase chemistry, particle-phase chemistry or some combination (Donahue et al., 2011), and (2) if the average saturation vapor concentration of the accumulation mode is also this low.

4.3 Aerosol hygroscopicity

In this section, we focus on the hygroscopicity of the particles that were measured as CCN. Figure 10 shows CCN at 4 supersaturations as well as the number of particles larger than 100 nm (CN100), 150 nm (CN150) and 240 nm (CN240) measured by the SMPS at Raven's Nest. Since the SMPS does not count particles larger than 685 nm, these CN estimates are biased low; however, the number concentrations of particles >685 nm is insignificant to this discussion (Macdonald et al., 2012). The CCN at all supersaturations as well as the CN100, CN150 and CN240 drop slightly on 5 July before the new particle formation and

Table 1. Particle growth analysis. Date refers to the day nucleation began. Growth rate and survival probability are calculated from that day through the end of 9 July (unless the nucleation modes grew out of the size ranges given below before the end).

Day	Date	Avg. growth rate (20–40 nm) (nm h ⁻¹)		Survival Probability (16–100 nm)	
		Model	Measurements	Model	Measurements
1	5 July	2.5	1.63	0.59	0.48
2	6 July	0.75	0.68	0.15	0.11
3	7 July	1.25	1.96	0.06	0.03
4	8 July	1.86	1.37	0.01	0
5	9 July	2.8	0.76	0	0

Day	Date	Avg. growth rate (1–20nm) (nm h ⁻¹)		Survival Probability (1–100 nm)	
		Model	Measurements	Model	Measurements
1	5 July	3.1	N/A	0.24	N/A
2	6 July	1.4	N/A	0.11	N/A
3	7 July	2.4	N/A	0.01	N/A
4	8 July	4.8	N/A	0	N/A
5	9 July	2.9	N/A	0	N/A

growth by organic condensation starts to influence the CCN and accumulation-mode sizes particles. Starting on 6 July, the concentration of CCN with supersaturations of 0.2 % and higher, CN100 and CN150 grow steadily with time through 8 July. CCN at 0.1 % supersaturation (CCN(0.1 %)) and CN240 stay fairly constant throughout this period, with some increase of CCN(0.1 %) on 8 July.

From about 7 July onward, CN240 and CCN(0.1 %) track each other well. If the aerosols at each size are internally mixed (e.g. if all particles with diameters close to 240 nm have the same composition), which should be the case since the mountain valley is away from large primary particle source, the critical diameter for 0.1 % supersaturation must correspond to a diameter very close to 240 nm. This critical diameter at 0.1 % supersaturation corresponds to an overall hygroscopicity factor (κ ; Petters and Kreidenweis, 2007) of about 0.11. This κ value includes the influence of small amounts of sulfate. Figure 11 shows 12-h averaged size-resolved sulfate and organic signals from the HR-AMS for the morning of 7 July and the evening of 8 July. Sulfate contributes about 3 % of the mass for particles larger than 240 nm on 7 July and 2 % on 8 July, and we assume the sulfate had a κ of 0.65. In order to get closure between size-distribution and composition derived CCN and the measured CCN, the organic κ is calculated to be 0.10. Similarly, the CN150 and CCN(0.2 %) track each other closely during this same period, which means the critical diameter for 0.2 % supersaturation is about 150 nm. This also corresponds to an overall κ of 0.11 and a similar organic κ of 0.10. This consistency of κ between the two supersaturations implies that the hygroscopicity of organics in 150 and 240 nm particles were similar. From 5 July to the afternoon of 7 July, the CN100 and CCN(0.3 %) track each other closely, which corresponds

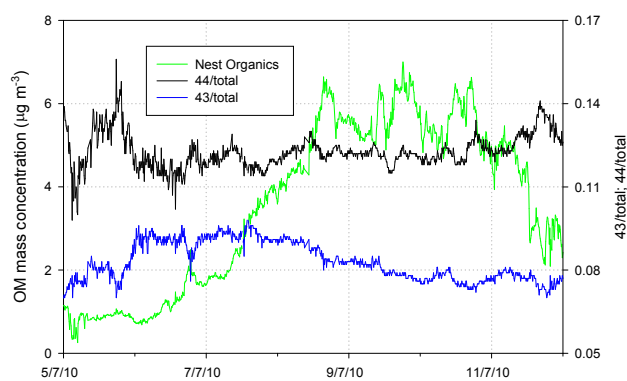


Fig. 12. Timeseries of AMS total organics, and the ratios of mass-to-charge 43 and mass-to-charge 44 to total organics measured at Raven's Nest.

to a critical diameter of 100 nm for 0.3 % supersaturation and a more hygroscopic κ of 0.17 than for the larger particles. However, from the afternoon of 7 July onward, the CCN(0.3 % and 0.5 %) track significantly below the CN100, which corresponds to a κ less than 0.06. The size-resolved AMS composition during this time period (Fig. 11) shows that the sulfate was substantially diminished (at or below detection limit) in the 100 nm sized particles after 7 July, presumably due to the continued growth of the particles by SOA condensation. Figure 12 shows that at about the same time the AMS-measured ratio of m/z -44 (an oxidized fragment of the OM components) to the total OM dropped, and although the ratio of m/z -44 to total OM increased afterwards until about midday on 8 July, the ratio of m/z -43 (a somewhat less oxidized fragment of the OM components) to the total

OM continued to decrease steadily from about midday on 7 July. These reductions in sulfate and the changes in the oxygenated components of the OM likely contributed to the reduced CN activity of the 100 nm particles (assuming that the change in composition of the 100 nm particle was similar to change for all particles measured by the AMS). In addition, it is possible that volatilization of OM within the CCN chamber that was several degrees above ambient may also have reduced the apparent CCN activity of the CN100 (e.g. Asa-Awuku et al., 2009).

The κ value of 0.1 found for the particles with diameters larger than 150 nm agrees well with the estimates of the ambient Whistler aerosol in Wong et al. (2011) as well as with other estimates of moderately oxidized atmospheric OM summarized in Wong et al. (2011).

4.4 Contribution to CCN concentrations

In Figs. 2 and 8, the new particles appear to grow effectively to CCN sizes (diameter > 100 nm). Whether or not a new particle will grow to become a CCN is determined primarily by a competition between condensational growth and coagulation with larger particles (Pierce and Adams, 2007). Kuang et al. (2009) and Westervelt et al. (2011) have analyzed the survival probabilities of freshly nucleated particles growing to 100 nm within one day of nucleation at other locations. The survival probability is the likelihood that a particle of a given size will grow to a larger size through condensation or coagulation with smaller particles before the particle in question coagulates with a larger particle. They found that the probability of growth from diameters smaller than 3 nm to 100 nm to vary greatly between locations, with median probabilities between 1 %–2 % in most locations to 10 % in the Po Valley in Italy.

We quantify the growth rates and the survival probabilities of growing to larger sizes for both the SMPS measurements and the model results using the technique described in Westervelt et al. (2011), which draws upon growth rate and nucleation rate estimation techniques from (Dal Maso et al., 2005) and survival probability estimation techniques from Pierce and Adams (2007). The results are highlighted in Table 1. For each of the particle formation events from 5 July through 9 July, the technique tracks the new particles' mode as it grows until the end of 9 July. Table 1 shows the mean growth rate between 20–40 nm and survival probability of 16 nm particles growing to 100 nm calculated from observations at Raven's Nest as well as from the TOMAS model. 100 nm is used as a surrogate for CCN-sized particles at higher supersaturations (see the previous section regarding CCN and particle size). Because the observations are limited to particles with diameters larger than 16 nm, we cannot calculate the survival probability from nucleation (~ 1 nm) to 100 nm from the observations. However, we can calculate this probability for the TOMAS model, so we include the mean growth rates from 1–16 nm and the survival probability of freshly

nucleated 1 nm particles growing to 100 nm for the TOMAS model.

The average growth rates between 20–40 nm range from 0.5 to 3 nm h⁻¹ (depending on day) for both the model and observations at Raven's Nest. These growth rates are for the time when the particles are between 20 nm and 40 nm, which can include periods of slower growth (e.g. nighttime), and thus these numbers are lower than the peak growth rates during SOA formation bursts. For example, the growth between 1–16 nm is closer to the time when nucleation occurred and thus when photochemical production is high. The predicted growth between 1–16 nm in the model is as high as 5 nm h⁻¹, though even this too may include periods of slower growth.

The survival probabilities between 16–100 nm agree well for the model and observations. The new particles on 5 July have the highest probability of growing to become CCN (48 % observed and 59 % modeled) because the pre-existing condensation and coagulation sinks are low (Fig. 7b). This means that the new particles get a larger fraction of condensable material on this day as well as having the lowest rate of coagulation scavenging. The probabilities decrease to 11 % observed and 15 % modeled for the new particles on 6 July, and 3 % observed and 6 % modeled for the new particles on 7 July. By the last two analyzed days, the survival probability is effectively 0 in the measurements and 1 % or lower in the model due to the large condensation/coagulation sinks and having a smaller amount of time to grow.

We used the model to estimate the fraction of nucleated ($D_p \sim 1$ nm) particles that survive to grow to 100 nm. The particles that formed on 5 July have a 28 % chance of growing to become CCN. Survival probabilities drop to 11 % on 6 July, 1 % on 7 July and essentially 0 % on the final two days because these small particles are very susceptible to coagulation by the growing coagulation sink. In Westervelt et al. (2011), median measured survival probabilities for 1 nm particles growing to 100 nm for single day nucleation and growth events were between 1 and 10 %, with a maximum observed survival probability above 50 % from one event at the Po Valley in Italy. The majority of the nucleation events tested in that work have much lower survival probabilities than reported here, although not considering multi-day growth in Westervelt et al. (2011) may skew survival probabilities low. Regardless, it is clear that the nucleation on 5 and 6 July 2010 at Whistler was a relatively efficient source of CCN-sized particles due to the relatively high levels of biogenic VOCs and fast condensation rates of the SOA from the VOC oxidation. This shows that even when the continental boundary layer is dominated by natural chemistry, CCN can be formed very efficiently from new-particle formation.

5 Conclusions

In this paper we investigated nucleation, growth and CCN properties during an extended biogenic SOA event during the Whistler Aerosol and Cloud Study (WACS 2010) between 5–10 July 2010. In-situ measurements were at two locations on Whistler Mountain in British Columbia, Canada. The event was characterized by relatively low concentrations of SO₂, sulfate and other inorganic species.

Concentrations of 20–30 nm particles were observed to increase each afternoon during the biogenic event – albeit most strongly at the beginning of the biogenic period. Our analyses show that even though the SO₂ concentrations were at or near the detection limit (0.05 ppbv), the source of the new particles could be explained by boundary-layer nucleation theories developed to match observations in other continental locations. We cannot explain why the particles are not observed by the SMPS before they are ~20 nm; however, it may be because of (1) nucleation and growth to 20 nm occurring in the nighttime residual layer or free troposphere that are entrained into the mixed layer during the afternoon, or (2) nucleation and growth happening at near the valley floor with mixing up to the mountain measurement sites in the afternoon as the mixed layer grows in depth. Although we had measurements at two elevations on Whistler mountain, we did not notice a difference in the timing of the onset of the particles between the two locations (to within ~10 min), which would have given clues to the source location, but we did see slightly smaller particles at the lower site. This negligible difference is likely due to fast mixing and upslope flows during the daytime boundary layer. Future studies would require particle flux measurements (e.g. Nilsson et al., 2001), balloon-borne CPC measurements (e.g. Laakso et al., 2007; Lauros et al., 2011) or aircraft measurements (e.g. O'Dowd et al., 2009) to gain more insight into the nature of the new particles.

We find that the OC condensing on the ultrafine particles must be low volatility with saturation concentrations of about 10⁻³ μg m⁻³ or less. This is consistent with the results of Pierce et al. (2011), which determined this volatility at other locations. The hygroscopicity parameter, κ , of the organic aerosol during the event was found to be about 0.1 for particles with diameters larger than ~150 nm. These κ values are consistent with the estimates of Wong et al. (2011) during the same study using a different technique. For smaller (~100 nm) particles, the observed κ value varied from 0.17 to <0.06. This change in κ occurred after sulfate grew out of the 100-nm particle size range (due to organic condensation) leaving nearly pure organic particles. Also during this same time period, the fraction of oxidized organic aerosol decreased. These two reasons may be partially responsible for the decrease in organic κ .

Although there was very little sulfate formation for growing the freshly nucleated particles, the condensing organics very efficiently grew the particles to CCN sizes. We

predicted that about 24% and 11% of the particles that nucleated during the first two days of the event, respectively, grew to 100 nm before being scavenged by coagulation. These values are significantly higher than most previously observed values. The growth probabilities on the later days of the event were much lower primarily due to larger condensation and coagulation sinks.

The results of this paper show that nucleation/growth can be an effective source of continental CCN in the general absence of anthropogenic pollution. Although we must recognize that while this case was chosen due to the larger-than-normal amounts of organic aerosol at Whistler, it shows that only a small amount of SO₂ is necessary to initiate CCN formation through nucleation and growth. This study gives insight into the potential properties and life cycle of pre-industrial aerosols under similar conditions.

Acknowledgements. Environment Canada funded the Whistler Aerosol and Cloud Study 2010 through the Clean Air Regulatory Agenda (CARA). Funding was provided through Environment Canada's Grants and Contribution program for JRP and CDW (G&C 1004966), LMR and LA (G&C 1004953), and JPDA, AKYL, and JPSW (G&C 1004932). Co-operation and support from Whistler-Blackcomb is gratefully acknowledged. JPDA, AKYL and JPSW were also funded by the Canadian Foundation for Climate and Atmospheric Science (CFCAS).

Edited by: A. Nenes

References

- Adams, P. J. and Seinfeld, J. H.: Predicting global aerosol size distributions in general circulation models, *J. Geophys. Res.*, 107, 4370, doi:10.1029/2001JD001010, 2002.
- Albrecht, B. A.: Aerosols, Cloud Microphysics, and Fractional Cloudiness, *Science*, 245, 1227–1230, 1989.
- Asa-Awuku, A., Engelhart, G. J., Lee, B. H., Pandis, S. N., and Nenes, A.: Relating CCN activity, volatility, and droplet growth kinetics of β -caryophyllene secondary organic aerosol, *Atmos. Chem. Phys.*, 9, 795–812, doi:10.5194/acp-9-795-2009, 2009.
- Canagaratna, M. R., Jayne, J. T., Jimenez, J. L., Allan, J. D., Alfarra, M. R., Zhang, Q., Onasch, T. B., Drewnick, F., Coe, H., Middlebrook, A. M., Delia, A., Williams, L. R., Trimborn, A. M., Northway, M. J., DeCarlo, P. F., Kolb, C. E., Davidovits, P., and Worsnop, D. R.: Chemical and microphysical characterization of ambient aerosols with the Aerodyne aerosol mass spectrometer, *Mass Spectrom. Rev.*, 26, 185–222, 2007.
- Chang, R. Y.-W., Slowik, J. G., Shantz, N. C., Vlasenko, A., Liggi, J., Sjostedt, S. J., Leaitch, W. R., and Abbatt, J. P. D.: The hygroscopicity parameter (κ) of ambient organic aerosol at a field site subject to biogenic and anthropogenic influences: relationship to degree of aerosol oxidation, *Atmos. Chem. Phys.*, 10, 5047–5064, doi:10.5194/acp-10-5047-2010, 2010.
- Dal Maso, M., Kulmala, M., Riipinen, I., Wagner, R., Hussein, T., Aalto, P. P., and Lehtinen, K. E. J.: Formation and growth of fresh atmospheric aerosols: eight years of aerosol size distribution data from SMEAR II, Hyytiälä, Finland, *Boreal Environ. Res.*, 10, 323–336, 2005.

- DeCarlo, P. F., Kimmel, J. R., Trimborn, A., Northway, M. J., Jayne, J. T., Aiken, A. C., Gonin, M., Fuhrer, K., Horvath, T., Docherty, K. S., Worsnop, D. R., and Jimenez, J. L.: Field Deployable, High-Resolution, Time-of-Flight Aerosol Mass Spectrometer, *Anal. Chem.*, 78, 8281–8289, 2006.
- DeCarlo, P. F., Dunlea, E. J., Kimmel, J. R., Aiken, A. C., Sueper, D., Crouse, J., Wennberg, P. O., Emmons, L., Shinzuka, Y., Clarke, A., Zhou, J., Tomlinson, J., Collins, D. R., Knapp, D., Weinheimer, A. J., Montzka, D. D., Campos, T., and Jimenez, J. L.: Fast airborne aerosol size and chemistry measurements above Mexico City and Central Mexico during the MILAGRO campaign, *Atmos. Chem. Phys.*, 8, 4027–4048, doi:10.5194/acp-8-4027-2008, 2008.
- Donahue, N. M., Robinson, A. L., Stanier, C. O., and Pandis, S. N.: Coupled partitioning, dilution, and chemical aging of semivolatile organics, *Environ. Sci. Technol.*, 40, 2635–2643, 2006.
- Donahue, N. M., Trump, E. R., Pierce, J. R., and Riipinen, I.: Theoretical Constraints on Pure Vapor-Pressure Driven Condensation of Organics to Ultrafine Particles, *Geophys. Res. Lett.*, 38, L16801, doi:10.1029/2011GL048115, 2011.
- Drewnick, F., Hings, S. S., DeCarlo, P. F., Jayne, J. T., Gonin, M., Fuhrer, K., Weimer, S., Jimenez, J. L., Demerjian, K. L., Borrmann, S., and Worsnop, D. R.: A new Time-of-Flight Aerosol Mass Spectrometer (ToF-AMS) – Instrument description and first field deployment, *Aerosol Sci. Tech.*, 39, 637–658, 2005.
- Epstein, S. A., Riipinen, I., and Donahue, N. M.: A Semiempirical Correlation between Enthalpy of Vaporization and Saturation Concentration for Organic Aerosol, *Environ. Sci. Technol.*, 44, 743–748, 2010.
- Forster, P., Ramaswamy, V., Artaxo, P., Berntsen, T., Betts, R., Fahey, D. W., Haywood, J., Lean, J., Lowe, D. C., Myhre, G., Nganga, J., Prinn, R., Raga, G., Schulz, M., and Dorland, R. V.: Changes in Atmospheric Constituents and in Radiative Forcing, in: *Climate Change 2007: The Physical Science Basis. Contribution of Working Group I to the Fourth Assessment Report of the Intergovernmental Panel on Climate Change*, edited by: Miller, H. L., Cambridge University Press, Cambridge, United Kingdom and New York, NY, USA, 2007.
- Gallagher, J. P., McKendry, I. G., Cottle, P. W., Macdonald, A. M., Leaitch, W. R., and Strawbridge, K.: Seasonal and Diurnal Variations in Aerosol Concentration on Whistler Mountain: Boundary Layer Influence and Synoptic Scale Controls, *J. Appl. Meteorol.*, in press, 2011.
- Goldstein, A. H. and Galbally, I. E.: Known and Unexplored Organic Constituents in the Earth's Atmosphere, *Environ. Sci. Technol.*, 41, 1514–1521, 2007.
- Hallquist, M., Wenger, J. C., Baltensperger, U., Rudich, Y., Simpson, D., Claeys, M., Dommen, J., Donahue, N. M., George, C., Goldstein, A. H., Hamilton, J. F., Herrmann, H., Hoffmann, T., Iinuma, Y., Jang, M., Jenkin, M. E., Jimenez, J. L., Kiendler-Scharr, A., Maenhaut, W., McFiggans, G., Mentel, Th. F., Monod, A., Prévôt, A. S. H., Seinfeld, J. H., Surratt, J. D., Szmigielski, R., and Wildt, J.: The formation, properties and impact of secondary organic aerosol: current and emerging issues, *Atmos. Chem. Phys.*, 9, 5155–5236, doi:10.5194/acp-9-5155-2009, 2009.
- Jayne, J. T., Leard, D. C., Zhang, X. F., Davidovits, P., Smith, K. A., Kolb, C. E., and Worsnop, D. R.: Development of an Aerosol Mass Spectrometer for Size and Composition Analysis of Submicron Particles, *Aerosol Sci. Tech.*, 33, 49–70, 2000.
- Jimenez, J. L., Jayne, J. T., Shi, Q., Kolb, C. E., Worsnop, D. R., Yourshaw, I., Seinfeld, J. H., Flagan, R. C., Zhang, X. F., Smith, K. A., Morris, J. W., and Davidovits, P.: Ambient Aerosol Sampling with an Aerosol Mass Spectrometer, *J. Geophys. Res.*, 108, 8425, doi:10.1029/2001JD001213, 2003.
- Kanakidou, M., Seinfeld, J. H., Pandis, S. N., Barnes, I., Dentener, F. J., Facchini, M. C., Van Dingenen, R., Ervens, B., Nenes, A., Nielsen, C. J., Swietlicki, E., Putaud, J. P., Balkanski, Y., Fuzzi, S., Horth, J., Moortgat, G. K., Winterhalter, R., Myhre, C. E. L., Tsigaridis, K., Vignati, E., Stephanou, E. G., and Wilson, J.: Organic aerosol and global climate modelling: a review, *Atmos. Chem. Phys.*, 5, 1053–1123, doi:10.5194/acp-5-1053-2005, 2005.
- Kerminen, V.-M., Lihavainen, H., Komppula, M., Viisanen, Y., and Kulmala, M.: Direct observational evidence linking atmospheric aerosol formation and cloud droplet activation, *Geophys. Res. Lett.* 32, L14803, doi:10.1029/2005GL023130, 2005.
- Kuang, C., McMurry, P. H., and McCormick, A. V.: Determination of cloud condensation nuclei production from measured new particle formation events, *Geophys. Res. Lett.*, 36, L09822, doi:10.1029/2009GL037584, 2009.
- Kulmala, M. and Kerminen, V. M.: On the formation and growth of atmospheric nanoparticles, *Atmos. Res.*, 90, 132–150, 2008.
- Kulmala, M., Dal Maso, M., Mäkelä, J. M., Pirjola, L., Väkevä, M., Aalto, P. P., Miiikkulainen, P., Hämeri, K., and O'Dowd, C. D.: On the formation, growth and composition of nucleation mode particles, *Tellus B*, 53, 479–490, 2001.
- Kulmala, M., Vehkamäki, H., Petaja, T., Dal Maso, M., Lauri, A., Kerminen, V. M., Birmili, W., and McMurry, P. H.: Formation and growth rates of ultrafine atmospheric particles: a review of observations, *J. Aerosol Sci.*, 35, 143–176, 2004.
- Kumar, P., Fennell, P., Symonds, J., and Britter, R. E.: Treatment of losses of ultrafine aerosol particles in long sampling tubes during ambient measurements, *Atmos. Environ.*, 42, 8819–8826, 2008.
- Laakso, L., Grönholm, T., Kulmala, L., Haapanala, S., Hirsikko, A., Lovejoy, E. R., Kazil, J., Kurtén, T., Boy, M., Nilsson, E. D., Sogachev, A., Riipinen, I., Stratmann, F., and Kulmala, M.: Hot-air balloon as a platform for boundary layer profile measurements during particle formation, *Boreal Environ. Res.*, 12, 279–294, 2007.
- Laaksonen, A., Hamed, A., Joutsensaari, J., Hiltunen, L., Cavalli, F., Junkermann, W., Asmi, A., Fuzzi, S., and Facchini, M. C.: Cloud condensation nucleus production from nucleation events at a highly polluted region, *Geophys. Res. Lett.* 32, L06812, doi:10.1029/2004GL022092, 2005.
- Lauros, J., Sogachev, A., Smolander, S., Vuollekoski, H., Sihto, S.-L., Mammarella, I., Laakso, L., Rannik, Ü., and Boy, M.: Particle concentration and flux dynamics in the atmospheric boundary layer as the indicator of formation mechanism, *Atmos. Chem. Phys.*, 11, 5591–5601, doi:10.5194/acp-11-5591-2011, 2011.
- Leaitch, W. R., MacDonald, A. M., Brickell, P. C., Liggió, J., Sjöstedt, S. J., Vlasenko, A., Bottenheim, J. W., Huang, L., Li, S.-M., Liu, P. S. K., Toom-Sauntry, D., Hayden, K. A., Sharma, S., Shantz, N. C., Wiebe, H. A., Zhang, W., Abbatt, J. P. D., Slowik, J. G., Chang, R. Y.-W., Russell, L. M., Schwartz, R. E., Takahama, S., Jayne, J. T., and Ng, N. L.: Temperature response of the submicron organic aerosol from temperate forests, *Atmos.*

- Environ., 45, 6696–6704, doi:10.1016/j.atmosenv.2011.08.047, 2011.
- Lihavainen, H., Kerminen, V. M., Komppula, M., Hatakka, J., Aaltonen, V., Kulmala, M., and Viisanen, Y.: Production of “potential” cloud condensation nuclei associated with atmospheric new particle formation in northern Finland, *J. Geophys. Res.-Atmos.*, 108, 4782, doi:10.1029/2003jd003887, 2003.
- Liu, B. Y. H., Romay, F. J., Dick, W. D., Woo, K. S., and Chiruta, M.: A Wide-Range Particle Spectrometer for Aerosol Measurement from 0.010 μm to 10 μm , *Aerosol Air Qual. Res.*, 10, 125–139, 2010.
- Macdonald, A. M., Anlauf, K. G., Leaitch, W. R., Chan, E., and Tarasick, D. W.: Interannual variability of ozone and carbon monoxide at the Whistler high elevation site: 2002–2006, *Atmos. Chem. Phys.*, 11, 11431–11446, doi:10.5194/acp-11-11431-2011, 2011.
- Macdonald, A. M., Leaitch, W. R., Abbatt, J. P. D., Ahlm, L., Al-Basheer, W., Betram, A. K., Buller, J., Campuzano-Jost, P., Chan, E., Corbin, J., Cziczo, D. J., Elford, A., Hayden, K. L., Herckes, P., Lee, A. K. Y., Li, S.-M., Liggio, J., Liu, P. S. K., Mihele, C., Noone, K. J., Pierce, J. R., Russell, L. M., Toom-Saunty, D., Schroder, J., Sharma, S., Sheppard, A., Sjostedt, S. J., Slowik, J. G., Strawbridge, K., Stuppel, G., Vlasenko, A., Wainwright, C. D., Wang, Y., Wentzell, J., Allan Wiebe, H., and Wong, J. P. S.: An Overview of WACS 2010: Biogenic Aerosol Formation, Mountain Flows and CCN, *Atmos. Chem. Phys.*, in preparation, 2012.
- Makkonen, R., Asmi, A., Korhonen, H., Kokkola, H., Järvenoja, S., Räisänen, P., Lehtinen, K. E. J., Laaksonen, A., Kerminen, V.-M., Järvinen, H., Lohmann, U., Bennartz, R., Feichter, J., and Kulmala, M.: Sensitivity of aerosol concentrations and cloud properties to nucleation and secondary organic distribution in ECHAM5-HAM global circulation model, *Atmos. Chem. Phys.*, 9, 1747–1766, doi:10.5194/acp-9-1747-2009, 2009.
- Merikanto, J., Spracklen, D. V., Mann, G. W., Pickering, S. J., and Carslaw, K. S.: Impact of nucleation on global CCN, *Atmos. Chem. Phys.*, 9, 8601–8616, doi:10.5194/acp-9-8601-2009, 2009.
- Metzger, A., Verheggen, B., Dommen, J., Duplissy, J., Prevot, A. S. H., Weingartner, E., Riipinen, I., Kulmala, M., Spracklen, D. V., Carslaw, K. S., and Baltensperger, U.: Evidence for the role of organics in aerosol particle formation under atmospheric conditions, *P. Natl. Acad. Sci. USA*, 107, 6646–6651, 2010.
- Nilsson, E. D., Rannik, Ü., Kulmala, M., Buzorius, G., and O’Dowd, C. D.: Effects of continental boundary layer evolution, convection, turbulence, entrainment, on aerosol formation, *Tellus B*, 53, 441–461, 2001.
- O’Dowd, C. D., Yoon, Y. J., Junkermann, W., Aalto, P., Kulmala, M., Lihavainen, H., and Viisanen, Y.: Airborne measurements of nucleation mode particles II: boreal forest nucleation events, *Atmos. Chem. Phys.*, 9, 937–944, doi:10.5194/acp-9-937-2009, 2009.
- Petäjä, T., Mauldin III, R. L., Kosciuch, E., McGrath, J., Nieminen, T., Paasonen, P., Boy, M., Adamov, A., Kotiaho, T., and Kulmala, M.: Sulfuric acid and OH concentrations in a boreal forest site, *Atmos. Chem. Phys.*, 9, 7435–7448, doi:10.5194/acp-9-7435-2009, 2009.
- Petters, M. D. and Kreidenweis, S. M.: A single parameter representation of hygroscopic growth and cloud condensation nucleus activity, *Atmos. Chem. Phys.*, 7, 1961–1971, doi:10.5194/acp-7-1961-2007, 2007.
- Pierce, J. R. and Adams, P. J.: Efficiency of cloud condensation nuclei formation from ultrafine particles, *Atmos. Chem. Phys.*, 7, 1367–1379, doi:10.5194/acp-7-1367-2007, 2007.
- Pierce, J. R. and Adams, P. J.: Uncertainty in global CCN concentrations from uncertain aerosol nucleation and primary emission rates, *Atmos. Chem. Phys.*, 9, 1339–1356, doi:10.5194/acp-9-1339-2009, 2009a.
- Pierce, J. R. and Adams, P. J.: A Computationally Efficient Aerosol Nucleation/Condensation Method: Pseudo-Steady-State Sulfuric Acid, *Aerosol Sci. Tech.*, 43, 1–11, 2009b.
- Pierce, J. R., Riipinen, I., Kulmala, M., Ehn, M., Petäjä, T., Junninen, H., Worsnop, D. R., and Donahue, N. M.: Quantification of the volatility of secondary organic compounds in ultrafine particles during nucleation events, *Atmos. Chem. Phys.*, 11, 9019–9036, doi:10.5194/acp-11-9019-2011, 2011.
- Riipinen, I., Sihto, S.-L., Kulmala, M., Arnold, F., Dal Maso, M., Birmili, W., Saarnio, K., Teinilä, K., Kerminen, V.-M., Laaksonen, A., and Lehtinen, K. E. J.: Connections between atmospheric sulphuric acid and new particle formation during QUEST III–IV campaigns in Heidelberg and Hyytiälä, *Atmos. Chem. Phys.*, 7, 1899–1914, doi:10.5194/acp-7-1899-2007, 2007.
- Riipinen, I., Pierce, J. R., Yli-Juuti, T., Nieminen, T., Häkkinen, S., Ehn, M., Junninen, H., Lehtipalo, K., Petäjä, T., Slowik, J., Chang, R., Shantz, N. C., Abbatt, J., Leaitch, W. R., Kerminen, V.-M., Worsnop, D. R., Pandis, S. N., Donahue, N. M., and Kulmala, M.: Organic condensation: a vital link connecting aerosol formation to cloud condensation nuclei (CCN) concentrations, *Atmos. Chem. Phys.*, 11, 3865–3878, doi:10.5194/acp-11-3865-2011, 2011.
- Roberts, G. and Nenes, A.: A Continuous-Flow Streamwise Thermal-Gradient CCN Chamber for Atmospheric Measurements, *Aerosol Sci. Tech.*, 39, 206–221, doi:10.1080/027868290913988, 2005.
- Seinfeld, J. H. and Pandis, S. N.: *Atmospheric Chemistry and Physics*, 2nd Edn., John Wiley and Sons, New York, 2006.
- Sihto, S.-L., Kulmala, M., Kerminen, V.-M., Dal Maso, M., Petäjä, T., Riipinen, I., Korhonen, H., Arnold, F., Janson, R., Boy, M., Laaksonen, A., and Lehtinen, K. E. J.: Atmospheric sulphuric acid and aerosol formation: implications from atmospheric measurements for nucleation and early growth mechanisms, *Atmos. Chem. Phys.*, 6, 4079–4091, doi:10.5194/acp-6-4079-2006, 2006.
- Spracklen, D. V., Carslaw, K. S., Kulmala, M., Kerminen, V.-M., Sihto, S.-L., Riipinen, I., Merikanto, J., Mann, G. W., Chipperfield, M. P., Wiedensohler, A., Birmili, W., and Lihavainen, H.: The contribution of particle formation to global cloud condensation nuclei concentrations, *Geophys. Res. Lett.*, 35, L06808, doi:10.1029/2007GL033038, 2008.
- Spracklen, D. V., Carslaw, K. S., Merikanto, J., Mann, G. W., Reddington, C. L., Pickering, S., Ogren, J. A., Andrews, E., Baltensperger, U., Weingartner, E., Boy, M., Kulmala, M., Laakso, L., Lihavainen, H., Kivekäs, N., Komppula, M., Mihalopoulos, N., Kouvarakis, G., Jennings, S. G., O’Dowd, C., Birmili, W., Wiedensohler, A., Weller, R., Gras, J., Laj, P., Sellegri, K., Bonn, B., Krejci, R., Laaksonen, A., Hamed, A., Minikin, A., Harrison, R. M., Talbot, R., and Sun, J.: Explaining global surface aerosol number concentrations in terms of primary emissions

- and particle formation, *Atmos. Chem. Phys.*, 10, 4775–4793, doi:10.5194/acp-10-4775-2010, 2010.
- Stevens, R. G., Pierce, J. R., Brock, C. A., Reed, M. K., Crawford, J. H., Holloway, J. S., Ryerson, T. B., Huey, L. G., and Nowak, J. B.: Nucleation and growth of sulfate aerosol in coal-fired power plant plumes: sensitivity to background aerosol and meteorology, *Atmos. Chem. Phys.*, 12, 189–206, doi:10.5194/acp-12-189-2012, 2012.
- Twomey, S.: The Influence of Pollution on the Shortwave Albedo of Clouds, *J. Atmos. Sci.*, 34, 1149–1152, 1977.
- Wang, M. and Penner, J. E.: Aerosol indirect forcing in a global model with particle nucleation, *Atmos. Chem. Phys.*, 9, 239–260, doi:10.5194/acp-9-239-2009, 2009.
- Wang, S. C. and Flagan, R. C.: Scanning Electrical mobility spectrometer, *Aerosol Sci. Tech.*, 13, 230–240, 1990.
- Westervelt, D. M., Riipinen, I., Pierce, J. R., Trivittayanurak, W., and Adams, P. J.: Formation, Growth, and Cloud Condensation Nuclei Production of Nucleated Particles: Comparison of Observations to a Global Aerosol Microphysics Model, *Atmos. Chem. Phys.*, in preparation, 2011.
- Wong, J. P. S., Lee, A. K. Y., Slowik, J. G., Cziczo, D. J., Leaitch, W. R., Macdonald, A., and Abbatt, J. P. D.: Oxidation of ambient biogenic secondary organic aerosol by hydroxyl radicals: Effects on cloud condensation nuclei activity, *Geophys. Res. Lett.*, 38, L22805, doi:10.1029/2011GL049351, 2011.
- Yu, F. and Luo, G.: Simulation of particle size distribution with a global aerosol model: contribution of nucleation to aerosol and CCN number concentrations, *Atmos. Chem. Phys.*, 9, 7691–7710, doi:10.5194/acp-9-7691-2009, 2009.